CrystEngComm

ROYAL SOCIETY OF CHEMISTRY

PAPER

View Article Online
View Journal | View Issue

Cite this: *CrystEngComm*, 2025, **27**, 4947

Wet-chemical approach to the synthesis of iron whitlockite ($Ca_{18}Fe_2(HPO_4)_2(PO_4)_{12}$) *via* a dissolution–precipitation process under hydrothermal conditions†

Diana Griesiute,[a] Jonas Stadulis,[a] Agne Kizalaite,[a] Andris Antuzevics,[ab] Arita Dubnika,[cd] Dominika Zakutna,[e] Vaclav Tyrpekl,[e] Chen-Ying Su,[fg] Hsu-Wei Fang[fg] and Aleksej Zarkov *[a]

Received 26th February 2025,
Accepted 15th June 2025

DOI: 10.1039/d5ce00207a

rsc.li/crystengcomm

In the present work, iron whitlockite (Fe-WH, $Ca_{18}Fe_2(HPO_4)_2(PO_4)_{12}$) powder was successfully synthesized by a wet-chemical approach. The synthesis was performed through a dissolution–precipitation process under hydrothermal conditions. The final product was obtained in a time-efficient manner *via* a phase conversion from $CaHPO_4{\cdot}2H_2O$ at 230 °C in just 1 h. Structural properties of the obtained material were comprehensively characterized by X-ray diffraction analysis and FTIR, Raman, and EPR spectroscopy. It was determined that in the as-prepared material, Fe ions mainly exist in a reduced divalent state in accordance with the peculiarities of the WH crystal structure. Magnetic studies also revealed paramagnetic behavior of Fe-WH in the temperature range from 5 to 300 K. Upon annealing, the Fe-WH structure decomposed, forming Fe-doped β-$Ca_3(PO_4)_2$ and $Ca_2P_2O_7$. Thermally induced decomposition was accompanied by the oxidation of Fe^{2+} to Fe^{3+}. The biocompatibility of the synthesized material was assessed by *in vitro* cytotoxicity experiments with the MC3T3-E1 preosteoblastic cell line. The investigated Fe-WH powder did not show a cytotoxic effect on the cells at all studied concentrations, demonstrating its high biocompatibility.

1. Introduction

Calcium phosphates (CPs) are a family of materials widespread in nature, both in biological and geological systems.[1] These materials are of particular importance for humans since the hard tissues of human beings are made of CPs, namely calcium hydroxyapatite (HA).[2] The chemical similarity with biological calcified tissues makes synthetic CPs highly biocompatible, which in turn leads to the use of these materials in medicine for various applications, including bone regeneration and reconstruction, gene delivery, bioimaging, *etc.*[2,3]

In literature, the name "whitlockite" is commonly referred to as magnesium whitlockite (Mg-WH, $Ca_{18}Mg_2(HPO_4)_2(PO_4)_{12}$), which can be considered as Mg-substituted CP. This mineral can be found both in the human body and in nature.[4,5] The WH of biological origin is assumed to be pure Mg-WH; however, there is a lack of data on the chemical analysis of this biomineral; therefore, the presence of other divalent ions in its structure cannot be excluded. The geological WH found in nature also contains some other elements besides Mg^{2+} ions, such as Na^+, Sr^{2+}, Fe^{2+}, Mn^{2+} *etc.*[4]

In recent decades, synthetic Mg-WH has attracted attention with the perspective of using this material in regenerative medicine. As a result, various synthetic approaches were demonstrated for preparing Mg-WH in the form of powders,[6–10] granules,[11] and composites.[12,13] Further biological studies indicated that in some cases, Mg-WH-based materials demonstrate superior properties compared to those of the most commonly used CPs such as HA or tricalcium phosphate (TCP, $Ca_3(PO_4)_2$).[13–18]

[a] *Institute of Chemistry, Vilnius University, Naugarduko 24, LT-03225 Vilnius, Lithuania. E-mail: aleksej.zarkov@chf.vu.lt*
[b] *Institute of Solid State Physics, University of Latvia, Kengaraga 8, LV-1063 Riga, Latvia*
[c] *Institute of Biomaterials and Bioengineering, Faculty of Natural Sciences and Technology, Riga Technical University, LV-1007 Riga, Latvia*
[d] *Baltic Biomaterials Centre of Excellence, Headquarters at Riga Technical University, LV-1658 Riga, Latvia*
[e] *Department of Inorganic Chemistry, Charles University, 128 00 Prague, Czech Republic*
[f] *High-Value Biomaterials Research and Commercialization Center, National Taipei University of Technology, Taipei 10608, Taiwan*
[g] *Department of Chemical Engineering and Biotechnology, National Taipei University of Technology, Taipei 10608, Taiwan*

† Electronic supplementary information (ESI) available. See DOI: https://doi.org/10.1039/d5ce00207a

More recently, studies on the synthesis and application of transition metal (TM) WH were published, reporting the preparation and application of Zn-, Cu-, Co-, and Mn-WH ($(Ca_{18}M_2(HPO_4)_2(PO_4)_{12})$, M = Zn^{2+}, Cu^{2+}, Co^{2+}, Mn^{2+}).[19–25] In these materials, the WH structure is stabilized by relatively small first-row TM ions instead of Mg^{2+}. One more member of divalent TM ions is Fe^{2+}; however, according to our knowledge, there are no papers describing the synthesis of iron whitlockite (Fe-WH, $Ca_{18}Fe_2(HPO_4)_2(PO_4)_{12}$) powders by wet chemical approaches. It is worth noting that Fe is redox-active, which can lead to the spontaneous oxidation of Fe^{2+} to Fe^{3+} in the reaction environment,[26] bringing additional difficulties to the synthesis of Fe-WH, where Fe ions should be present in their reduced oxidation state. According to our knowledge, currently, there is only one published article reporting the synthesis and characterization of deuterated Fe-WH powder.[27] In that work, the target material was prepared by a two-step procedure, which includes a high-temperature solid-state synthesis of $Ca_9Fe(PO_4)_7$ (Fe oxidation state is +3) with its further transformation to Fe-WH at elevated temperature in a reducing atmosphere.

Iron is not only an essential element in the human body, involved in numerous physiological processes, but also possesses magnetic properties, which can be employed for different biomedical applications. Particularly, magnetic Fe-substituted CPs or CP-based composites attracted scientific interest due to their potential application in magnetic hyperthermia, drug delivery, magnetic resonance imaging (MRI), *etc.*[28–34] Various Fe-substituted CPs and their composites were prepared and characterized in recent decades. For instance, Iafisco *et al.*[33] employed a superparamagnetic composite of Fe-doped HA and Fe_3O_4 as a delivery system for the anticancer drug doxorubicin. The application of magnetic field resulted in an increased release of the drug. A similar composite was demonstrated as a suitable agent for MRI, opening new prospects for the design of theranostic agents for personalized medical applications.[28] Duraisamy *et al.*[30] fabricated a multifunctional $NiFe_2O_4$-calcium fluorapatite composite with magnetic and antibacterial properties. Under tumor-mimicking conditions, the prepared composite achieved a hyperthermia temperature of *ca.* 43 °C; moreover, it was considered to be a promising drug delivery agent. Ribeiro *et al.*[32] determined HA substituted with mixed-valent Fe ions as pH-sensitive and biodegradable peroxidase-like nanozymes for cancer chemodynamic therapy and MRI. Taking into account the aforementioned properties of Fe-containing phosphates and their composites, Fe-WH can be considered as a more beneficial candidate for biomedical applications such as magnetic hyperthermia, drug delivery, or MRI, when compared to Mg-WH.

Our work aims to study Fe-WH as a member of the CP family, which is poorly investigated. First of all, we were interested in the feasibility of forming this material by a wet-chemical process in an aqueous medium. Further comprehensive characterization of structural, morphological, magnetic, and cytotoxic properties was performed, opening new horizons for using Fe-WH for biomedical applications.

2. Experimental

2.1. Synthesis

The synthesis of Fe-WH powder was performed through a dissolution-precipitation process under hydrothermal conditions. Dicalcium phosphate dihydrate (DCPD, $CaHPO_4{\cdot}2H_2O$, 99.1%, Eurochemicals) and iron sulfate heptahydrate ($FeSO_4{\cdot}7H_2O$, ≥99.5%, Roth) were used as starting materials. In a typical procedure, appropriate amounts of $CaHPO_4{\cdot}2H_2O$ and $FeSO_4{\cdot}7H_2O$ were dissolved in a mixture of 30 mL of deionized water and 30 mL of 1M phosphoric acid (H_3PO_4, 75%, Roth) in a 90 mL Teflon liner. The molar Ca-to-Fe ratio in the above mixture was equal to 9, and the total metal ion concentration was 0.42 mol L^{-1}. After the complete dissolution of precursors, the pH value of the obtained mixture was adjusted to 6.2 with an ammonia solution (NH_4OH, 25%, Roth) under constant mixing on a magnetic stirrer. The increase in the pH value resulted in the instantaneous formation of precipitates. Next, the obtained mixture was sealed in a stainless steel container and placed into an oven preheated to 230 °C for 1 h. The reaction time was calculated as a period from the placement of the container into the oven to the moment it was removed to room temperature. After the reaction, the precipitates were vacuum filtered, washed with deionized water, and dried at 80 °C in the oven.

2.2. Characterization

Powder X-ray diffraction (XRD) data of the synthesized powders were obtained using a Rigaku MiniFlex II diffractometer (Cu-K_α, λ = 1.5419 Å) working in the Bragg–Brentano ($\theta/2\theta$) geometry. The data were collected within the 10–100° 2θ angle range with a speed of 1° min^{-1}. The FullProf suite was employed for structural refinement (FullProf suite software version September-2020). Fourier transform infrared (FTIR) spectra were taken in the 400–4000 cm^{-1} range (30 scans) with a Bruker ALPHA-FTIR spectrometer. Raman spectra were recorded using a combined Raman and scanning near-field optical microscope WiTec Alpha 300 R equipped with a 532 nm excitation laser source. The measurements were performed with 600 g mm^{-1} diffraction grating, pixel resolution of <3 cm^{-1}, the integration time was 1 s, the number of scans was 50 and the approximate laser power of 15 mW. The morphology of the synthesized specimens was studied by scanning electron microscopy (SEM) using a Hitachi SU-70 microscope. Magnetic susceptibility data for Fe-WH were collected using a Quantum Design MPMS3 SQUID magnetometer. The data collection involved a temperature sweep ranging from 5 K to 300 K at a magnetic field strength of 100 Oe under both zero-field cooled (ZFC) and field-cooled (FC) conditions. Magnetic hysteresis data were collected at 5 K and 300 K over a range of −20 000 Oe to 20 000 Oe. Data collection was performed

either in vibrating sample magnetometry (VSM) mode with 5 mm scan lengths and 2 s averaging or in direct current (DC) scan mode with 30 mm scan lengths and 5 s averaging. A Bruker ELEXSYS-II E500 CW-EPR spectrometer was used for electron paramagnetic resonance (EPR) investigations of the samples. The spectra acquisition settings were: room temperature, 9.839 GHz (X-band) or 34.00 GHz (Q-band) microwave frequency, 1 mW microwave power, and 0.4 mT magnetic field modulation amplitude. Elemental composition of the Fe-WH powder was determined by inductively coupled plasma optical emission spectrometry (ICP-OES) using a Perkin-Elmer Optima 7000 DV spectrometer. The sample was dissolved in 5% nitric acid (HNO_3, Rotipuran® Supra 69%, Carl Roth) and diluted to appropriate volume. Calibration solutions were prepared by an appropriate dilution of the stock standard solutions (single-element ICP standards 1000 mg L^{-1}, Carl Roth).

2.3. *In vitro* cytotoxicity studies

The cytotoxicity of the Fe-WH powder was evaluated using the MC3T3-E1 preosteoblast cell line. For the extract test, 4500 cells per well were seeded in a 96-well plate with 100 μL of cell culture medium, which consisted of 89% Alpha Modified Eagle Medium (α-MEM), 10% fetal bovine serum (FBS), and 1% penicillin/streptomycin (P/S). The plates were incubated overnight at 37 °C with 5% CO_2 (New Brunswick™ S41i CO_2 Incubator Shaker, Eppendorf, Hamburg, Germany).

Fe-WH powder was suspended in 5 mL of fresh cell culture medium to achieve a 10 mg mL^{-1} concentration. After 24 and 48 h, the entire solution was collected and replaced with another 5 mL of fresh cell culture medium. The collected solution was filtered through a 0.2 μm syringe filter and then diluted with fresh medium to concentrations of 1 mg mL^{-1}, 0.1 mg mL^{-1}, and 0.01 mg mL^{-1}. These extract dilutions were immediately added to the preincubated cells (100 μL per well). Untreated cells served as the positive control, while cells treated with a 5% dimethylsulfoxide (DMSO) solution in the medium served as the negative control. Each sample and control conditions were tested in six replicates.

Cytotoxicity of the Fe-WH extracts was assessed using a Cell Counting Kit-8 (CCK-8) assay. Samples were incubated for 24 h for both time points, after which 10 μL of CCK-8 solution was added to each well and incubated for 1 h at 37 °C with 5% CO_2. Absorbance at 450 nm was measured using an Infinite M Nano microplate reader (Tecan, Männedorf, Switzerland).

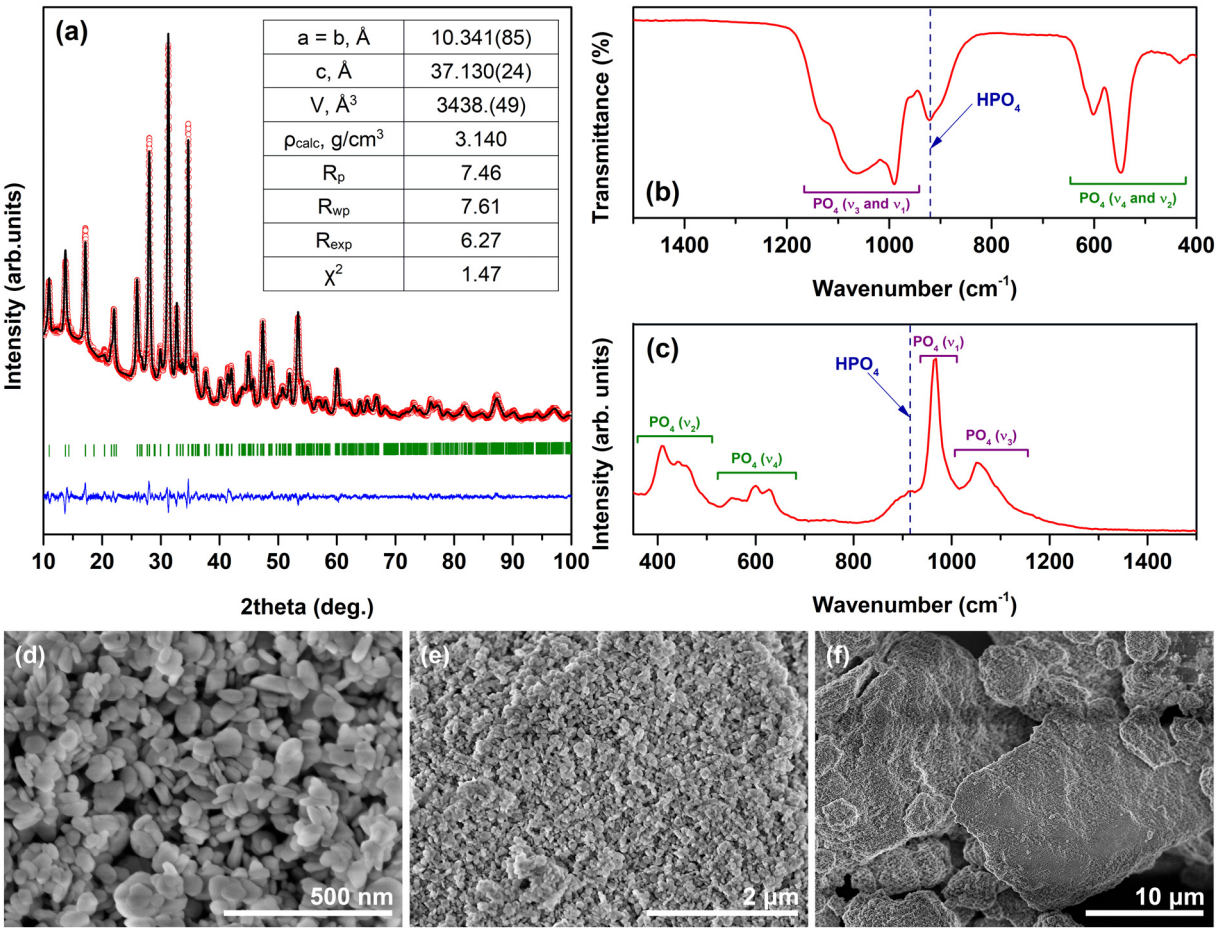

Fig. 1 XRD pattern (a); FTIR spectrum (b); Raman spectrum (c); and SEM micrographs (d–f) of the Fe-WH powder.

3. Results and discussion

The as-precipitated powder (without hydrothermal treatment) was analyzed by means of XRD analysis, and the crystalline phase was identified as DCPD (Fig. S1†), which is in good agreement with the previous data on the dissolution-precipitation synthesis of Zn-WH.[20] However, a broad signal centered at *ca.* 30° suggests that the amorphous component also co-exists in the sample. The XRD analysis of the as-prepared Fe-WH did not indicate the presence of secondary crystalline phases (Fig. 1a). All diffraction peaks matched very well with the standard XRD data of Mg-WH (#04-009-3397). There were no peaks corresponding to any impurity such as monetite or HA, which are commonly obtained secondary phases during the wet synthesis of WH materials.[20,35] Rietveld refinement was further performed using a rhombohedral structure with a space group *R3c* (#161) adopted from Mg-WH as a model. The results demonstrated a good agreement between the calculated and experimental data; the cell parameters were calculated as a = 10.341(85) Å and c = 37.130(24) Å. These values are close to those of Mg-, Zn- and Cu-WH synthesized by the wet chemical approach.[6,20,23] Overall, the lattice parameters of isostructural Mg-WH and divalent TM-WH are quite similar, which can be explained by the closeness of the ionic radii of Mg^{2+} and TM^{2+} ions.[36] In all cases, a small cation (Mg^{2+} or TM^{2+}) occupies the octahedral Ca(5) site, which is reasonable since this site has the smallest coordination number in the WH crystal structure. In our case, it was also determined that Fe^{2+} ions occupy the Ca(5) site (Fig. S2†). The agreement of the lattice parameters of our synthesized Fe-WH and literature data[4,20,37] can be considered as an indirect confirmation of the predominant divalent state of Fe ions. The parameters reported by Belik *et al.*[27] for the deuterated analog of Fe-WH, namely $Ca_{18}Fe_2(DPO_4)_2(PO_4)_{12}$ were slightly larger.

FTIR and Raman spectroscopy are powerful tools for identifying the WH structure since these techniques allow observing the absorption band corresponding to the HPO_4^{2-} group. The presence of this spectral marker confirms the formation of WH but excludes related structures such as Fe-doped β-TCP or $Ca_9Fe(PO_4)_7$, which do not contain this structural unit.[38] The FTIR spectrum of the Fe-WH powder is given in the representative range of 400–1500 cm^{-1} (Fig. 1b) since the materials with the WH structure do not show any bands in the rest part of the spectrum up to 4000 cm^{-1}. Three groups of absorption bands can be highlighted: the bands located in the range from *ca.* 1200 to 945 cm^{-1} correspond to v_3 and v_1 stretching modes of the phosphate tetrahedra; while the bands ranging from 500 to 650 cm^{-1} and the band centered at 430 cm^{-1} are ascribed to v_4 and v_2 bending modes, respectively;[19,39] finally, the band centered at 920 cm^{-1} represents the HPO_4^{2-} unit.[6,7] A remarkable feature of the observed FTIR spectrum is the width of the band at 920 cm^{-1}, which was significantly broader compared to that observed for Mg- and TM-WH reported in previous works.[6,20,23] Corresponding bands were also observed in the Raman spectrum in the ranges of approximately 370–510 cm^{-1} (v_2), 530–655 cm^{-1} (v_4), and 1100–1200 cm^{-1} (v_3) (Fig. 1c); the most intense band peaked at 965 cm^{-1} is attributed to the v_1 symmetric stretching mode.[40] The band assigned to the HPO_4^{2-} group located at *ca.* 920 cm^{-1} is clearly visible in the spectrum;[41,42] however, it is not perfectly resolved due to overlapping with the v_1 band. Similarly, like in the FTIR spectrum, the bands in the Raman spectrum are very broad compared to previously reported data on both synthetic[20] and especially natural WH.[42] A possible reason for the broadening could be the low crystallinity of the synthesized material. The relatively low intensity of the v_1 band also could be attributed to the low crystallinity. Alternatively, the presence of Fe^{3+} defects in the crystal lattice of Fe-WH could lead to the distortion of crystal structure and broadening of the bands. Overall, the results of both spectroscopic techniques are in good agreement and confirm the formation of the Fe-WH structure.

The SEM images of the Fe-WH powder depict the formation of well-defined plate-like particles varying in size from approximately 40 to 100 nm (Fig. 1d). The polygonal shape of the particles is characteristic of WH materials; however, the formation of a particular shape depends on many parameters, including the synthetic approach, concentration of starting materials, the ratio of metal cations, *etc.*[7,9,19,20] The SEM micrographs taken under lower magnification indicate the aggregation of individual particles to large agglomerates of micrometric dimensions (Fig. 1e and f).

The elemental analysis of the Fe-WH powder was performed by means of ICP-OES to determine the chemical composition of the synthesized material (Table 1). The theoretical values were calculated according to the $Ca_{18}Fe_2(HPO_4)_2(PO_4)_{12}$ formula, which assumes that Fe ions are exclusively divalent. Overall, the experimental data agree very well with the theoretical data; however, the experimentally determined Ca/Fe ratio was slightly higher than that of the theoretical data, while the determined (Ca + Fe)/P molar ratio was slightly lower compared to that of the theoretical data. This observation is compatible with the hypothesis that a minor part of the Fe ions is oxidized to the trivalent state; although, the discrepancies are insignificant. Moreover, the presence of minor amorphous impurities, influencing the composition of the bulk material, cannot be excluded.

Table 1 Results of the elemental analysis of Fe-WH powder

Theoretical Ca/Fe molar ratio	Determined Ca/Fe molar ratio	Theoretical (Ca + Fe)/P molar ratio	Determined (Ca + Fe)/P molar ratio
9.00	9.16	1.43	1.40

We were also interested in the feasibility of synthesizing a mixed-valent Fe-WH containing comparable/significant amounts of both Fe^{2+} and Fe^{3+} ions. For this purpose, a mixture of divalent and trivalent iron precursors was used, namely $FeSO_4{\cdot}7H_2O$ and $Fe(NO_3)_3{\cdot}9H_2O$. A series of powders was synthesized, varying the ratio of Fe^{3+}/Fe^{2+} in the initial reaction mixture from 0 to 100 mol% with a step of 20 mol%. The results demonstrated that the presence of Fe^{3+} ions moved the phase equilibrium toward the formation of HA (Fig. S3†). The presence of 20 mol% of Fe^{3+} already resulted in the formation of biphasic material consisting of Fe-WH and HA, while HA was a dominant phase when a higher amount of Fe^{3+} was used. These results indicate that by varying the iron precursors, the phase composition of the final product can be tuned; however, the co-existence of a significant amount of both Fe^{3+} and Fe^{2+} in the crystal structure of Fe-WH was impossible to achieve. On the other hand, previous works demonstrated that the WH structure is stabilized exclusively by relatively small divalent ions. To our knowledge, there are no reports on preparing the WH structure containing only Ca^{2+} and trivalent ions. By contrast, a successful synthesis of Fe^{2+}/Fe^{3+}-doped HA was previously reported in the literature, indicating a better ability of the HA crystal structure to adopt aliovalent ions compared to WH.[26,43]

Magnetic properties of the synthesized Fe-WH powder were investigated by measuring the inverse magnetic susceptibility $1/\chi$ *vs.* T and the dependence of magnetization on the applied field. The $1/\chi$ *vs.* T curves obtained in both FC and ZFC modes are presented in Fig. 2a. The linear dependence was observed in both cases, reflecting a paramagnetic behavior of Fe-WH in the temperature range from 300 K down to 5 K. No difference between FC and ZFC curves was observed. The effective magnetic moment, $\mu_{eff} = (8C)^{1/2}$, was calculated as 5.07 μ_B (μ_B, Bohr magneton) per Fe^{2+} ion, which is only slightly higher compared to the theoretical value of 4.90 μ_B. The calculated μ_{eff} value can be assumed as a confirmation of the presence of Fe ions in a divalent state. The results agree with the data reported by Belik *et al.*[27] for $Ca_{18}Fe_2(DPO_4)_2(PO_4)_{12}$, who calculated the μ_{eff} value as 4.97 μ_B. The M *vs.* H curves, taken at 5 K and 300 K, also show an expected paramagnetic behavior demonstrating magnetization values of 6.7 and 0.19 emu g^{-1} at the magnetic field of 20 kOe at 5 K and 300 K, respectively (Fig. 2b).

Tuning of the magnetic properties of Fe-WH potentially could be achieved by the fabrication of Fe-WH composites with iron oxides. This approach was previously demonstrated by Tampieri *et al.*,[26] who investigated the composite of Fe-doped HA and iron oxides. It was shown that hyperthermia curves of undoped HA-Fe_3O_4 and Fe-doped HA-Fe_3O_4 differ significantly. The difference was ascribed to the potential interaction between two magnetic phases compared to a single magnetic material in HA-Fe_3O_4.

Both Mg- and TM-WH are known to be thermally unstable.[6,19,23,44] Upon annealing, these materials gradually decompose, forming ion-substituted β-TCP and $Ca_2P_2O_7$ (CPP). In terms of chemical bonds, this phase transformation leads to the formation of the P–O–P bond presenting in the CPP structure instead of the decomposed HPO_4^{2-} structural unit. The detailed study on the thermally-induced degradation of Mg-WH revealed a broad temperature range of the co-existence of 3 crystalline phases: WH, β-TCP, and CPP.[6] Moreover, it was shown that the information obtained from the XRD analysis is limited, since it allows only for determining the starting degradation temperature by detecting the appearance of the secondary CPP phase. This technique does not detect the end of the phase transformation due to the identical XRD patterns of WH and β-TCP.

It should be noted that in the case of Mg-, Zn-, or Cu-stabilized WH, the oxidation state of all composing elements is supposed to be the same after the thermal treatment; however, the situation is different in the case of redox-active Fe. At least two scenarios should be considered for the possible mechanism of thermally-induced degradation of Fe-

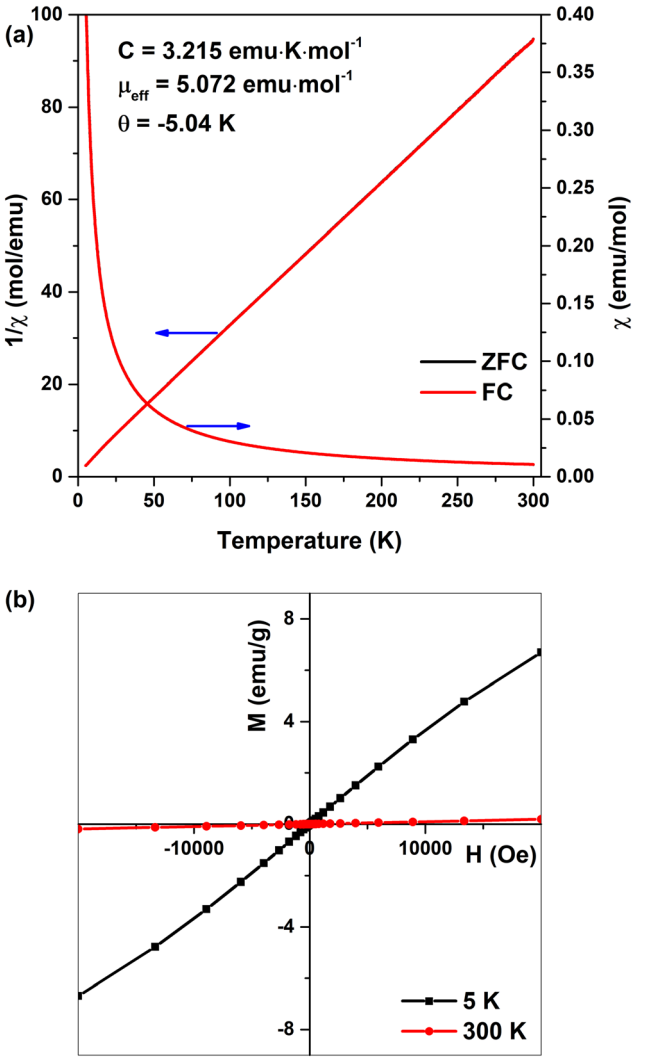

Fig. 2 Magnetic susceptibility and inverse magnetic susceptibility of Fe-WH *vs.* T (a); M *vs.* H curves of Fe-WH at 5 K and 300 K (b).

WH in the air atmosphere. The first scenario assumes the oxidation of Fe^{2+} to Fe^{3+} accompanied by the transformation of HPO_4^{2-} to exclusively PO_4^{3-} and H_2. In this case, the reaction should occur according to eqn (1), and the oxidation of Fe achieves the charge compensation. For this reaction, the XRD analysis will not show the appearance of new diffraction peaks.

$$Ca_{18}Fe_2(HPO_4)_2(PO_4)_{12} \rightarrow 2Ca_9Fe(PO_4)_7 + H_2 \quad (1)$$

The second potential scenario considers that the oxidation of Fe^{2+} occurs at temperatures exceeding those of the decomposition of HPO_4^{2-}, which would lead to the formation of PO_4^{3-} and $P_2O_7^{4-}$.

The representative XRD patterns of Fe-WH powders annealed at different temperatures are given in Fig. 3a (all XRD patterns for annealing temperatures from 500 °C to 1200 °C are shown in Fig. S4†). Annealing up to 600 °C did not produce new diffraction peaks; however, the XRD pattern of the powder annealed at 700 °C already contained some reflections corresponding to CPP. The temperature of the formation of CPP agrees well with the results obtained for Mg- and other TM-WH.[6,23] The annealing at higher temperatures showed no further significant changes except the narrowing of the diffraction peaks.

As a rule, the decomposition of the WH structure can be detected in FTIR spectra by simultaneous reduction of the intensity of the HPO_4^{2-}-related band and the appearance of the P–O–P absorption band centered at 726 or 754 cm^{-1}, characteristic of CPP.[45] For Mg-, Zn-, and Cu-WH, these processes occur gradually and start at around 600–700 °C.[6,20,23] Fig. 3b shows that the FTIR spectrum of Fe-WH considerably changes already after annealing at 500 °C. The absorption band ascribed to HPO_4^{2-} (*ca.* 920 cm^{-1}) disappeared. On the other hand, two new bands centered at 877 and 930 cm^{-1} were observed instead. Such behavior was not previously observed for Mg-, Zn- or Cu-WH. The reason for the drastic spectral change could be associated with the change in the oxidation state of Fe^{2+} ions. The appearance of the absorption bands centered at 726 and 756 cm^{-1} was observed only at 700 °C. These bands indicate the simultaneous formation of both α- and β-CPP polymorphs.[45] At higher annealing temperatures, only β-CPP was detected up to 1200 °C. The band observed at 877 cm^{-1} gradually shifted to the lower wavenumbers, peaking at 864 cm^{-1} for 900 °C.

Doping of a closely related β-TCP structure with aliovalent Fe^{3+} or Ga^{3+} ions modified the FTIR spectrum of β-TCP.[38,46,47] The absorption bands at 873 cm^{-1} and 871 cm^{-1} appeared with an increase of the dopant concentration in β-TCP prepared at 800 °C and 900 °C, respectively.[38,46] Overall, the spectrum of Fe-WH annealed at 500 °C is very similar to that of Fe^{3+}-doped β-TCP in terms of the shape and band positions.[38,46] These observations suggest that annealing at 500 °C causes the oxidation of Fe^{2+} to Fe^{3+}; however, it does not induce the transformation of HPO_4^{2-} structural unit to $P_2O_7^{4-}$, which occurs starting from *ca.* 700 °C. Thus, the degradation pathway could be assumed to be an intermediate between the abovementioned mechanisms. Previously, it was

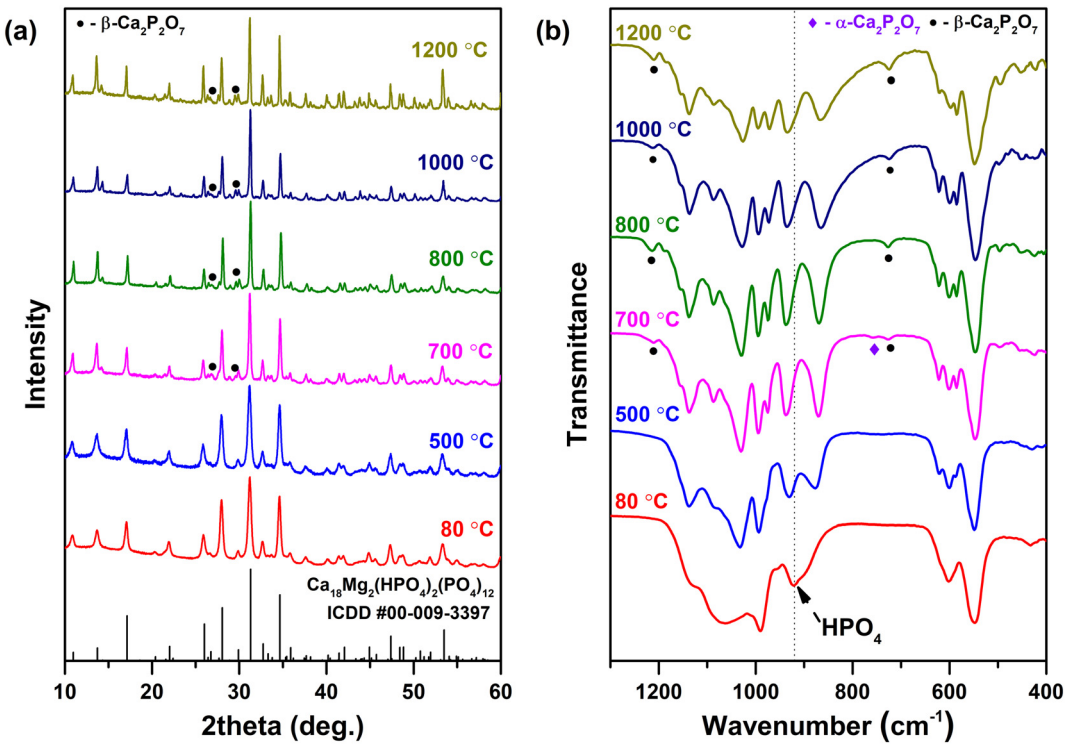

Fig. 3 XRD patterns (a) and FTIR spectra (b) of Fe-WH powders annealed at different temperatures.

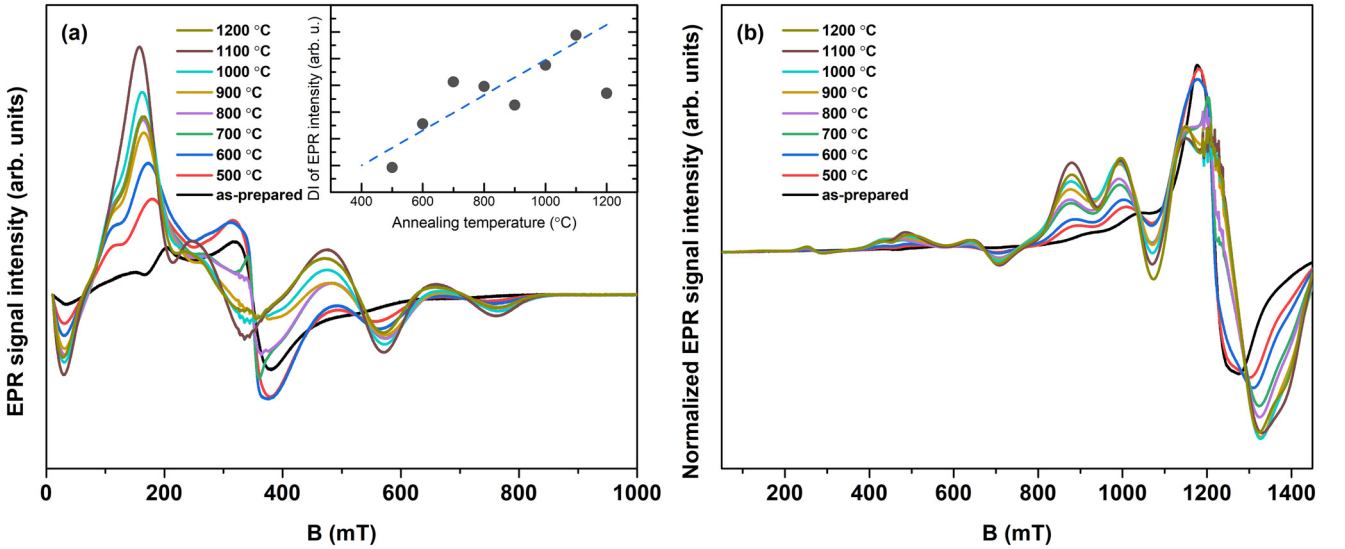

Fig. 4 X-band (a) and normalized Q-band (b) EPR spectra of the Fe-WH powders. Inset: double integral (DI) intensities of EPR spectra as a function of the sample annealing temperature.

demonstrated that ^{1}H and ^{31}P solid-state nuclear magnetic resonance is the most powerful tool in monitoring the phase transformation from Mg-WH to β-TCP;[6] unfortunately, in the case of Fe-WH, the use of this technique is impossible due to the presence of Fe ions.

EPR spectroscopy analysis of the investigated samples is presented in Fig. 4. The EPR spectra cover a broad magnetic field range and depend on the sample treatment temperature. Iron in the Fe^{3+} state is detectable in conventional EPR measurements at room temperature.[38,48–50] X-band EPR spectra, normalized to sample mass (Fig. 4a), can be used to compare the relative Fe^{3+} ion content in the samples. A Fe^{3+} signal can be detected in the as-prepared sample, possibly showing the presence of a minor amount of Fe^{3+} in the Fe-WH crystal lattice or a minor contribution of Fe^{3+}-rich impurity. EPR spectra double integral (DI) values, which are proportional to the number of paramagnetic centers, exhibit an increasing tendency up to 1100 °C annealing temperature. This increase in signal intensity is likely due to the oxidation of Fe^{2+} to Fe^{3+} during sample annealing in an air atmosphere.

Annealing also produces changes in the local structure of Fe^{3+} ions, which is evidenced by the variations in EPR signal shapes. This effect is illustrated in Fig. 4b, where Q-band EPR spectra are shown in a normalized representation. As EPR transitions of paramagnetic ions are sensitive to the coordination geometry with neighboring ligands, EPR spectra are helpful in monitoring structural transformations of materials. The EPR spectra of the annealed samples resemble those of Fe^{3+}-doped β-TCP,[38,49] which is consistent with the conclusion inferred from XRD and FTIR analysis that Fe-WH decomposes into β-TCP.

The cell viability of Fe-WH was evaluated in adherence to ISO 10993-5:2009 guidelines. Analysis indicated that none of the tested Fe-WH extract dilutions exhibited cytotoxic effects following a 24-hour incubation period at both 24 and 48 h timepoints (Fig. 5).

Two main observations can be highlighted from the examination of cell viability data. First, at the 24 h timepoint, slightly lower cell viability was observed for a higher concentration of Fe-WH (1 mg mL^{-1}). Second, the observed pattern suggests that cell viability declines across the lower Fe-WH dilutions (1 and 0.1 mg mL^{-1}) following a 48-hour incubation period. Nevertheless, the value remains consistently and noticeably above 70%, indicating that cytotoxic effects are not pronounced. A recent study by Predoi *et al.*[51] on amorphous iron-calcium phosphate nanoparticles showed that osteoblastic cell viability was dependent on the incubation period, and iron-containing CP coating promoted the proliferation and adhesion of the cells after 72 h of incubation. Furthermore, Wei *et al.*[52] studied the effect of

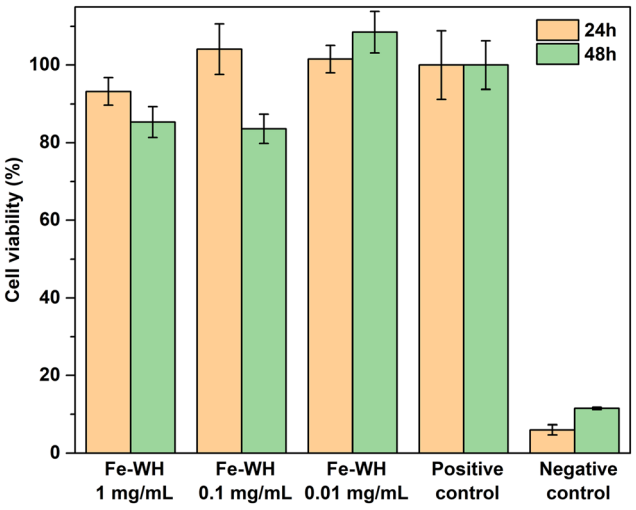

Fig. 5 Fe-WH extract effect on MC3T3-E1 cell proliferation.

collagen-coated composite of iron oxide nanospheres and Sr-substituted HA on the MC3T3-E1 preosteoblast cell line, showing increased gene expression and, thus, cell differentiation in the presence of the nanospheres. Cell viability and upregulation of the osteogenic and angiogenic genes are linked with the Fe concentration and release kinetics from the material since concentrations from 10 to 100 μM enhance angiogenesis, but excessive amounts can cause toxicity and ferroptosis.[53] Unfortunately, other studies on the biological properties of Fe-WH are currently absent for comparison; however, our results demonstrate the potential of Fe-WH for further studies in the biomedical field.

4. Conclusions

Iron whitlockite (Fe-WH, $Ca_{18}Fe_2(HPO_4)_2(PO_4)_{12}$) powder was successfully synthesized by a wet chemical approach under hydrothermal conditions in just 1 h. According to the XRD analysis, the obtained material was phase-pure, without any crystalline impurities. Rietveld refinement confirmed that Fe^{2+} ions occupy the Ca(5) site, which agrees well with the peculiarities of the WH crystal structure. The magnetic studies confirmed that in the as-prepared Fe-WH, Fe ions mostly exist in a reduced divalent state; however, the Fe^{3+} signal in the as-prepared sample was detected by EPR, possibly showing the presence of a minor amount of Fe^{3+} in the Fe-WH crystal lattice. The magnetic studies also revealed a paramagnetic behavior of Fe-WH in the temperature range from 5 to 300 K. Upon annealing, the Fe-WH structure decomposed, forming Fe-doped β-$Ca_3(PO_4)_2$ and $Ca_2P_2O_7$. Thermally induced decomposition was accompanied by the oxidation of Fe^{2+} to Fe^{3+}. The biocompatibility of the synthesized material was assessed by *in vitro* cytotoxicity experiments and did not show a cytotoxic effect on the cells at all studied concentrations, demonstrating its high biocompatibility.

Data availability

The data supporting this study have been included within the article and the corresponding ESI.†

Conflicts of interest

There are no conflicts to declare.

Acknowledgements

This project has received funding from the Research Council of Lithuania (LMTLT), agreement No S-MIP-23-85. The authors acknowledge the access to the infrastructure and expertise of the BBCE – Baltic Biomaterials Centre of Excellence (European Union's Horizon 2020 research and innovation programme under grant agreement No. 857287). Prof. S. L. Stoll, Dr. O. Stewart (Georgetown University) and Dr. T. Murauskas (Vilnius University) are highly acknowledged for their help with material characterization.

References

1 S. V. Dorozhkin and M. Epple, *Angew. Chem., Int. Ed.*, 2002, **41**, 3130–3146.
2 W. Habraken, P. Habibovic, M. Epple and M. Bohner, *Mater. Today*, 2016, **19**, 69–87.
3 M. Gu, W. Li, L. Jiang and X. Li, *Acta Biomater.*, 2022, **148**, 22–43.
4 F. Capitelli, F. Bosi, S. C. Capelli, F. Radica and G. Della Ventura, *Crystals*, 2021, **11**, 225.
5 F. A. Shah, *Acta Biomater.*, 2021, **125**, 72–82.
6 A. Kizalaite, V. Klimavicius, V. Balevicius, G. Niaura, A. N. Salak, J. C. Yang, S. H. Cho, T. Goto, T. Sekino and A. Zarkov, *CrystEngComm*, 2023, **25**, 4370–4379.
7 C. Wang, K.-J. Jeong, H. J. Park, M. Lee, S.-C. Ryu, D. Y. Hwang, K. H. Nam, I. H. Han and J. Lee, *J. Colloid Interface Sci.*, 2020, **569**, 1–11.
8 A. Afonina, A. Kizalaite, A. Zarkov, A. Drabavicius, T. Goto, T. Sekino, A. Kareiva and I. Grigoraviciute-Puroniene, *Ceram. Int.*, 2022, **48**, 32125–32130.
9 H. L. Jang, H. K. Lee, K. Jin, H.-Y. Ahn, H.-E. Lee and K. T. Nam, *J. Mater. Chem. B*, 2015, **3**, 1342–1349.
10 H. L. Jang, K. Jin, J. Lee, Y. Kim, S. H. Nahm, K. S. Hong and K. T. Nam, *ACS Nano*, 2014, **8**, 634–641.
11 W.-B. Lee, C. Wang, J.-H. Lee, K.-J. Jeong, Y.-S. Jang, J.-Y. Park, M. H. Ryu, U.-K. Kim, J. Lee and D.-S. Hwang, *ACS Appl. Bio Mater.*, 2020, **3**, 7762–7768.
12 X. Zhang, W. Liu, J. Liu, Y. Hu and H. Dai, *ACS Biomater. Sci. Eng.*, 2021, **7**, 3321–3331.
13 S. Pouraghaei Sevari, J. K. Kim, C. Chen, A. Nasajpour, C.-Y. Wang, P. H. Krebsbach, A. Khademhosseini, S. Ansari, P. S. Weiss and A. Moshaverinia, *ACS Appl. Mater. Interfaces*, 2021, **13**, 35342–35355.
14 H. L. Jang, G. B. Zheng, J. Park, H. D. Kim, H.-R. Baek, H. K. Lee, K. Lee, H. N. Han, C.-K. Lee, N. S. Hwang, J. H. Lee and K. T. Nam, *Adv. Healthcare Mater.*, 2016, **5**, 128–136.
15 D. Zhou, C. Qi, Y.-X. Chen, Y.-J. Zhu, T.-W. Sun, F. Chen and C.-Q. Zhang, *Int. J. Nanomed.*, 2017, **12**, 2673–2687.
16 H. D. Kim, H. L. Jang, H.-Y. Ahn, H. K. Lee, J. Park, E.-S. Lee, E. A. Lee, Y.-H. Jeong, D.-G. Kim, K. T. Nam and N. S. Hwang, *Biomaterials*, 2017, **112**, 31–43.
17 H. Cheng, R. Chabok, X. Guan, A. Chawla, Y. Li, A. Khademhosseini and H. L. Jang, *Acta Biomater.*, 2018, **69**, 342–351.
18 M. Hu, F. Xiao, Q.-F. Ke, Y. Li, X.-D. Chen and Y.-P. Guo, *Chem. Eng. J.*, 2019, **359**, 1–12.
19 A. Kizalaite, I. Grigoraviciute-Puroniene, D. R. C. Asuigui, S. L. Stoll, S. H. Cho, T. Sekino, A. Kareiva and A. Zarkov, *ACS Biomater. Sci. Eng.*, 2021, **7**, 3586–3593.
20 A. Kizalaite, V. Klimavicius, J. Versockiene, E. Lastauskiene, T. Murauskas, R. Skaudzius, T. Yokoi, M. Kawashita, T. Goto, T. Sekino and A. Zarkov, *CrystEngComm*, 2022, **24**, 5068–5079.
21 M. Wang, J. Yao, S. Shen, C. Heng, Y. Zhang, T. Yang and X. Zheng, *Nano Res.*, 2023, **16**, 757–770.

22 T. Konishi and S. Watanabe, *Phosphorus Res. Bull.*, 2022, **38**, 18–24.
23 D. Griesiute, A. Kizalaite, A. Dubnika, V. Klimavicius, V. Kalendra, V. Tyrpekl, S. H. Cho, T. Goto, T. Sekino and A. Zarkov, *Dalton Trans.*, 2024, **53**, 1722–1734.
24 S. Y. Stefanovich, B. I. Lazoryak, A. M. Antipin, A. S. Volkov, A. I. Evdokimov, O. A. Gurbanova, O. V. Dimitrova and D. V. Deyneko, *Z. fur Krist. - Cryst. Mater.*, 2023, **238**, 301–309.
25 C. Heng, W. Liu, X. Zheng, X. Ma, J. Hui and D. Fan, *Colloids Surf., B*, 2023, **222**, 113120.
26 A. Tampieri, T. D'Alessandro, M. Sandri, S. Sprio, E. Landi, L. Bertinetti, S. Panseri, G. Pepponi, J. Goettlicher, M. Bañobre-López and J. Rivas, *Acta Biomater.*, 2012, **8**, 843–851.
27 A. A. Belik, F. Izumi, S. Y. Stefanovich, B. I. Lazoryak and K. Oikawa, *Chem. Mater.*, 2002, **14**, 3937–3945.
28 A. Adamiano, M. Iafisco, M. Sandri, M. Basini, P. Arosio, T. Canu, G. Sitia, A. Esposito, V. Iannotti, G. Ausanio, E. Fragogeorgi, M. Rouchota, G. Loudos, A. Lascialfari and A. Tampieri, *Acta Biomater.*, 2018, **73**, 458–469.
29 B. Srinivasan, E. Kolanthai, N. E. A. Kumaraswamy, R. R. Jayapalan, D. S. Vavilapalli, L. H. Catalani, G. S. Ningombam, N. S. Khundrakpam, N. R. Singh and S. N. Kalkura, *J. Phys. Chem. B*, 2019, **123**, 5506–5513.
30 K. Duraisamy, A. Gangadharan, K. S. Martirosyan, N. K. Sahu, P. Manogaran and G. Easwaradas Kreedapathy, *ACS Appl. Bio Mater.*, 2023, **6**, 104–116.
31 T. M. Oliveira, F. C. B. Berti, S. C. Gasoto, B. Schneider, M. A. Stimamiglio and L. F. Berti, *Front. Med.*, 2021, **3**, 700266.
32 T. P. Ribeiro, B. Salgado, J. Pinto, P. C. Silva, J. A. M. Santos, J. A. Moreira, F. J. Monteiro and M. S. Laranjeira, *Mater. Today Chem.*, 2024, **35**, 101861.
33 M. Iafisco, C. Drouet, A. Adamiano, P. Pascaud, M. Montesi, S. Panseri, S. Sarda and A. Tampieri, *J. Mater. Chem. B*, 2016, **4**, 57–70.
34 H. Inam, S. Sprio, M. Tavoni, Z. Abbas, F. Pupilli and A. Tampieri, *Int. J. Mol. Sci.*, 2024, **25**, 2809.
35 A. Afonina, A. Dubauskas, V. Klimavicius, A. Zarkov, A. Kareiva and I. Grigoraviciute, *Ceram. Int.*, 2023, **49**, 38157–38164.
36 R. D. Shannon, *Acta Crystallogr., Sect. A*, 1976, **32**, 751–767.
37 R. Gopal, C. Calvo, J. Ito and W. K. Sabine, *Can. J. Chem.*, 1974, **52**, 1155–1164.
38 L. Sinusaite, A. Popov, A. Antuzevics, K. Mazeika, D. Baltrunas, J.-C. Yang, J. L. Horng, S. Shi, T. Sekino, K. Ishikawa, A. Kareiva and A. Zarkov, *Mater. Sci. Eng., C*, 2020, **112**, 110918.
39 R. G. Carrodeguas and S. De Aza, *Acta Biomater.*, 2011, **7**, 3536–3546.
40 P. N. de Aza, C. Santos, A. Pazo, S. de Aza, R. Cuscó and L. Artús, *Chem. Mater.*, 1997, **9**, 912–915.
41 B. Wopenka and J. D. Pasteris, *Mater. Sci. Eng., C*, 2005, **25**, 131–143.
42 B. L. Jolliff, J. M. Hughes, J. J. Freeman and R. A. Zeigler, *Am. Mineral.*, 2006, **91**, 1583–1595.
43 F. Pupilli, M. Tavoni, C. Drouet, A. Tampieri and S. Sprio, *Open Ceram.*, 2024, **18**, 100610.
44 V. K. Kaliannagounder, N. P. M. J. Raj, A. R. Unnithan, J. Park, S. S. Park, S.-J. Kim, C. H. Park, C. S. Kim and A. R. K. Sasikala, *Nano Energy*, 2021, **85**, 105901.
45 D. Griesiute, E. Raudonyte-Svirbutaviciene, A. Kareiva and A. Zarkov, *CrystEngComm*, 2022, **24**, 1166–1170.
46 R. K. Singh, M. Srivastava, N. K. Prasad, S. Awasthi, A. Dhayalan and S. Kannan, *Mater. Sci. Eng., C*, 2017, **78**, 715–726.
47 C. Mellier, F. Fayon, V. Schnitzler, P. Deniard, M. Allix, S. Quillard, D. Massiot, J.-M. Bouler, B. Bujoli and P. Janvier, *Inorg. Chem.*, 2011, **50**, 8252–8260.
48 B. Gabbasov, M. Gafurov, A. Starshova, D. Shurtakova, F. Murzakhanov, G. Mamin and S. Orlinskii, *J. Magn. Magn. Mater.*, 2019, **470**, 109–117.
49 D. Griesiute, L. Sinusaite, A. Kizalaite, A. Antuzevics, K. Mazeika, D. Baltrunas, T. Goto, T. Sekino, A. Kareiva and A. Zarkov, *CrystEngComm*, 2021, **23**, 4627–4637.
50 F. Murzakhanov, G. V. Mamin, S. Orlinskii, M. Goldberg, N. V. Petrakova, A. Y. Fedotov, P. Grishin, M. R. Gafurov and V. S. Komlev, *ACS Omega*, 2021, **6**, 25338–25349.
51 D. Predoi, S. L. Iconaru, S. C. Ciobanu, S.-A. Predoi, N. Buton, C. Megier and M. Beuran, *Coatings*, 2021, **11**, 186.
52 X. Wei, X. Zhang, Z. Yang, L. Li and H. Sui, *Arabian J. Chem.*, 2021, **14**, 102984.
53 M. A. Saghiri, A. Asatourian, J. Orangi, C. M. Sorenson and N. Sheibani, *Crit. Rev. Oncol. Hematol.*, 2015, **96**, 129–142.